JGR Planets

RESEARCH ARTICLE
10.1029/2022JE007669

The EUV Reflectance of Mercury's Surface Measured by BepiColombo/PHEBUS

J.-Y. Chaufray[1], E. Quémerais[1], D. Koutroumpa[1], R. Robidel[1], F. Leblanc[1], A. Réberac[1], I. Yoshikawa[2], K. Yoshioka[2], G. Murakami[3], O. Korablev[4], D. Belyaev[4], M. G. Pelizzo[5], and A. J. Corso[6]

[1]LATMOS-IPSL, CNRS, UVSQ, Paris-Saclay, Sorbonne Université, Guyancourt, France, [2]Tokyo University, Tokyo, Japan, [3]Institute of Space and Astronautical Science, Japan Aerospace Exploration Agency, Sagamihara, Japan, [4]IKI, Moscow, Russia, [5]Department of Information Engineering, University of Padova, Padova, Italy, [6]National Research Council of Italy, Institute for Photonics and Nanotechnologies, Padova, Italy

Key Points:

- We derive the reflectance of Mercury's surface between 90 and 160 nm for the first time since Mariner 10
- The lower albedo of Mercury compared to the Moon could be due to a lower FeO concentration but other opaque species may be needed
- Some spectral variations could possibly be due to SiO_2

Correspondence to:

J.-Y. Chaufray,
jean-yves.chaufray@latmos.ipsl.fr

Citation:

Chaufray, J.-Y., Quémerais, E., Koutroumpa, D., Robidel, R., Leblanc, F., Réberac, A., et al. (2023). The EUV reflectance of Mercury's surface measured by BepiColombo/PHEBUS. *Journal of Geophysical Research: Planets*, *128*, e2022JE007669. https://doi.org/10.1029/2022JE007669

Received 17 NOV 2022
Accepted 28 FEB 2023

Abstract

On 9 and 10 October 2021, Probing the Hermean Exosphere by Ultraviolet Spectroscopy aboard BepiColombo observed the disk-integrated reflected light from the Sun by Mercury in the spectral range 90–160 nm at a phase angle of 70°. These observations are used to derive the EUV reflectance of the surface of Mercury in this wavelength range for the first time since the Mariner 10 observations in 1974–1975. Our observations are in agreement with a surface of Mercury darker by a factor ∼0.5–0.6 compared to the Moon in this wavelength range, with an average reflectance of 0.3% at a phase angle of 70°. This lower reflectance of Mercury could be due to the lower abundance of FeO. The derived reflectance near 160 nm is close to the derived reflectance at 220 nm by MESSENGER/MASCS at a similar phase angle. Possible spectral variations measured between 110 and 140 nm could be attributed to SiO_2 glass, but the signal to noise ratio is low and other observations, possible at several periods during the rest of the cruise, are needed to confirm this last result.

Plain Language Summary

Due to the lack of atmosphere, the solar UV radiation directly impacts the surface of Mercury. A fraction of this radiation is reflected into space in all directions. This reflected fraction varies with wavelength and can be analyzed to constrain the composition and texture of the surface of Mercury. Probing the Hermean Exosphere by Ultraviolet Spectroscopy aboard BepiColombo observed the reflected radiation between 90 and 160 nm for the first time since the Mariner 10 observations in 1974–1975. In this study, we measure the fraction of UV radiation reflected at different wavelengths. We compare our results with past observations from Mariner 10. We explain part of the observed spectral variations as possible due to the presence of SiO_2 glass at the surface of Mercury and an albedo lower than the Moon due to a lower abundance of FeO.

1. Introduction

Spectral reflectance is a useful tool to investigate the composition of planetary surfaces. On the Moon, several variables affect the reflectance of surface including the amount of oxidation state of iron or titanium in silicates and oxides, the presence of opaque minerals such as ilmenite and carbon-bearing phases, and the degree of space weathering (e.g., Murchie et al., 2018). The presence of ferrous iron in minerals is responsible for an absorption band at ∼1 μm wavelength detected at the surface of the Moon (e.g., Hapke, 1977). On Mercury, this feature was not detected by Mariner 10 (Hapke, 1977), suggesting a lower abundance of ferrous oxides on Mercury than on the Moon. The lack of absorption band near ∼1 μm was confirmed by the observations performed by MESSENGER/MASCS (Izenberg et al., 2014; McClintock et al., 2008). This lack of detection has been used to estimate the fraction of FeO on Mercury with current estimate varying between (1%–5%) in agreement with the global range of ∼1%–2% and 1.3%–2.6% derived from MESSENGER's X-Ray Spectrometer (XRS) and Gamma-Ray Spectrometer (GRS) respectively (Domingue et al., 2014; Izenberg et al., 2014; Murchie et al., 2018; Vilas et al., 2016). The lower fraction of FeO on Mercury than on the Moon (varying between 3% at Tycho crater to 23% in the western mare regions Lawrence et al., 2002) is consistent with the reflectance shortward 200 nm of Mercury approximately ∼2/3 that of the Moon, derived by Mariner 10 (Hapke, 1977; Wu & Broadfoot, 1977). New UV measurements could provide new constrains on the FeO fraction at the surface of Mercury, even if a detailed quantification of the effect of FeO on the EUV albedo is still missing.

The UV reflectance of several airless bodies of the solar system has also been studied, showing the effect of the presence of ices on the Far-UV (FUV) reflectance (Gladstone et al., 2012; Hendrix et al., 2018) as well as the differences between fresh material and mature material of the same composition (Hendrix & Vilas, 2006; Hendrix, Retherford, et al., 2012), or specific regions like the swirls on the Moon (Hendrix et al., 2016). Sunlight can be scattered by two processes from a grain: reflection from the surface (Fresnel reflection) and volume scattering of rays which have been refracted into its interior (Hapke, 1981). At UV wavelengths, surface scattering can dominate because the grain size is typically much larger than the wavelength and the absorption increases toward shorter wavelengths (e.g., Hendrix & Vilas, 2006). Measuring the UV reflectance of a surface can then be used to provide constraints on the refractive index of the surface of the grains, considering, for example, a parametrized model of the bidirectional-reflectance (e.g., Hapke, 2001).

Remote observations are divided into two categories: disk-integrated and disk-resolved measurements (Domingue et al., 2010). Disk-integrated observations, studied in this paper, are a measure of the entire disk (disk-integrated reflectance) of Mercury. The disk-integrated reflectance depends on the solar phase angle g: the angle between the Sun-Mercury and Mercury-Observer directions (Hapke, 2012). Disk-integrated observations of Mercury have been conducted from Earth in the visible domain before the first flyby by Mariner 10 (Danjon, 1949; Irvine et al., 1968). Since these historical observations, disk-integrated observations of Mercury have been performed using Mariner 10 (see Cremonese et al., 2007 for a summary), SOHO (Mallama et al., 2002), and MESSENGER (Domingue et al., 2010; Holsclaw et al., 2010; McClintock et al., 2008). Mariner 10 observed the reflected solar flux at several wavelengths (58.4, 74, 86.7, 104.8, 121.6, 130.4, 148.0 and 165.7 nm) during the three flybys of Mercury (Wu & Broadfoot, 1977). A theoretical photometric function from Hapke (1966) was used to derive the physical (or geometric) albedo (i.e., the disk-integrated reflectance at 0° phase angle). The derived values were uncertain but found between 1%–4% with a general decrease from 58.4 to 165.7 nm.

MESSENGER observed the reflected solar flux longward of 200 nm (Domingue et al., 2010; Holsclaw et al., 2010; McClintock et al., 2008). The disk-integrated reflectance measured at phase angles of 75°, 86°, and 90° shows an increase of the reflectance from 220 to 300 nm by a factor of ∼3, larger than that of the Moon, without specific noticeable absorption feature (Holsclaw et al., 2010; McClintock et al., 2008).

In this study, we present new measurements of Mercury's reflectance acquired by Probing of Hermean Exosphere by Ultraviolet Spectroscopy (PHEBUS) (Chassefière et al., 2010; Quémerais et al., 2020) using the EUV channel (∼55–160 nm). The observations are presented in Section 2, the derived reflectance is presented in Section 3 and discussed in Section 4, followed by a conclusion in Section 5.

2. Methods

2.1. Observations

2.1.1. Instrumental Description

The PHEBUS instrument is a multiple channel instrument composed of two spectrographs operating in overlapping spectral ranges in the ultraviolet (EUV channel: 55–155 nm and FUV channel: 145–320 nm) and two additional band-integrating channels that capture emissions at 404 and 422 nm from potassium and calcium, respectively. The instrument and its scientific goals are described in detail in Chassefière et al. (2010) and Quémerais et al. (2020). Due to instrument functional constraints, only one of the 2 UV channels can be operated during one observation. The high-voltage of one channel needs to be ramped up before the measurements and then it is not possible to use a duty-cycle for two channels every 10 s. The two visible detectors can be activated along with the selected UV channel. Photons from the observed source pass through a rotating entrance baffle and reach the primary mirror. This rotating mechanism allows changing the pointing direction of the PHEBUS field of view (FOV). After reflection by the primary mirror, photons are focused on a removable rectangular slit (5.6 mm × 0.28 mm) placed at the focal plane (focal length = 170 mm) of the mirror (Quémerais et al., 2020) and reach one of the two holographic gratings (EUV and FUV). No imaging capability along the slit is possible. When the slit is removed, the projected field of PHEBUS is defined by the "pre-slit," which is the exit pupil of the scanner mechanism.

The EUV and FUV detectors are positioned along the focal planes of the gratings. In the UV ranges, the spectrum acquisition is accomplished by photon counting, detection is realized using a microchannel plate (MCP) with

Table 1
Geometric Parameter of the Six Observations of Mercury Done by Probing the Hermean Exosphere by Ultraviolet Spectroscopy

Sequence	Observation number	Date	D (AU)	Δ (AU)	Phase angle (degree)	$\Omega_{mercury}$ (str)	Scan angle
1	1	9 October 2021, 01:30:02–01:46:01	0.341	0.0271	68.2	1.13×10^{-6}	39.5°
	2	9 October 2021, 01:48:32–02:04:31	0.341	0.0271	68.2	1.13×10^{-6}	38.5°
	3	9 October 2021, 02:07:01–02:23:00	0.341	0.0272	68.3	1.13×10^{-6}	40.5°
2	4	9 October 2021, 23:30:02–23:46:01	0.336	0.0304	71.8	9.04×10^{-7}	160°
	5	9 October 2021, 23:48:32–00:04:31	0.336	0.0304	71.8	9.04×10^{-7}	159°
	6	10 October 2021, 00:07:01–00:23:00	0.336	0.0305	71.9	9.04×10^{-7}	161°

Note. D is the Sun-Mercury distance, Δ the BepiColombo-Mercury distance and $\Omega_{mercury}$ the solid angle of Mercury seen from BepiColombo.

Resistive Anode Encoder (RAE). In this manuscript, one observation will be defined as the measurements done continuously at one given scan angle.

2.1.2. Observations

Six observations using the EUV spectrograph were performed by PHEBUS on 9 and 10 October 2021 during two sequences. The first sequence was done on 9 October 2021 from 01:30 to 02:23 UT, using three different scan angles of PHEBUS equal to 39.5, 38.5 and 40.5° from the parking position (position of the instrument when it is not operating, see Quémerais et al., 2020 for details). This set of angles was selected to maximize the probability to have Mercury in the FOV of PHEBUS for at least one observation. The second sequence was done from 9 October 2021 23:30 to 10 October 00:23 using again three different scan angles (160°, 159°, 161°). The geometric parameters for each observation are given in Table 1. All the observations were performed without the slit, corresponding to an entrance FOV of 4.088 square degree (1.2×10^{-3} str), much larger than the size of Mercury seen from BepiColombo. For all these observations, Mercury can be considered as a point source. Possible small radiometric sensitivity of a few % with the scan angle is considered as part of a systematic uncertainty.

Mercury was detected during the six observations. Attempts to observe Mercury with the FUV detector during this period failed because of the use of nonoptimal detector parameters.

The 16 min-integrated images of the detector for each observation are shown in Figure 1.

The solar reflected light by the Mercury surface corresponds to the horizontal line near the center of the images. The different positions and inclinations of this horizontal line from one image to another are a consequence of the different positions of Mercury in the PHEBUS FOV. The signal is spread over horizontal rows 110–150. Above and below, only dark counts are observed (Quémerais et al., 2020).

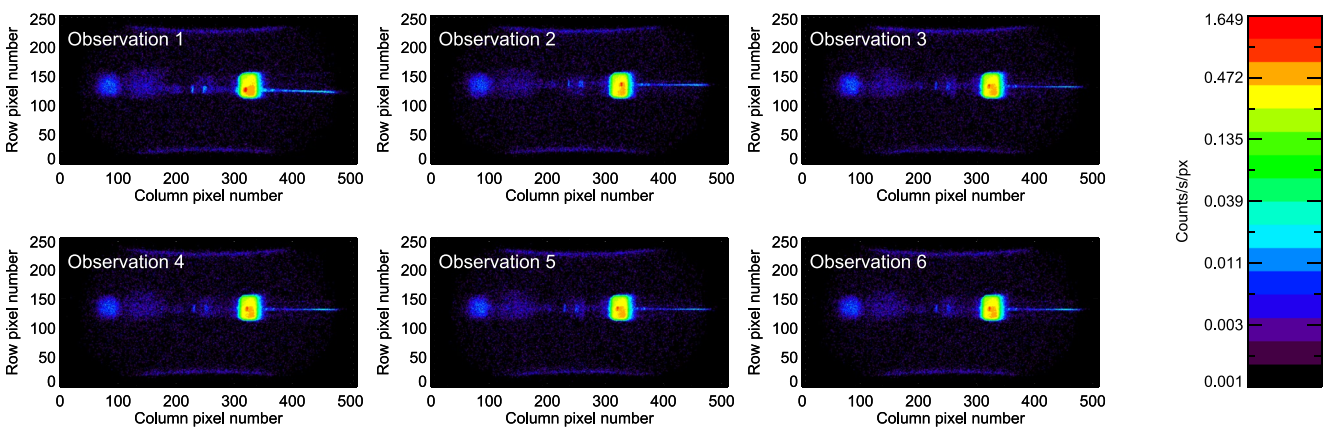

Figure 1. Images of the average count rate on the detector for the six observations. The spectral axis is the horizontal axis (the wavelength increases from left to right). The spectra are the sum of the reflected solar light by Mercury (bright nearly horizontal line in the middle of the image), the interplanetary medium (extended vertically spots with helium emission near column pixel 80 and Lyman-α near column pixel 320) and dark current. The two blue bended lines at the bottom and the top of each image are instrumental artifacts. The line spread function is not uniform and decreases with the wavelength. The maximum value is ∼1.65 count/px/s.

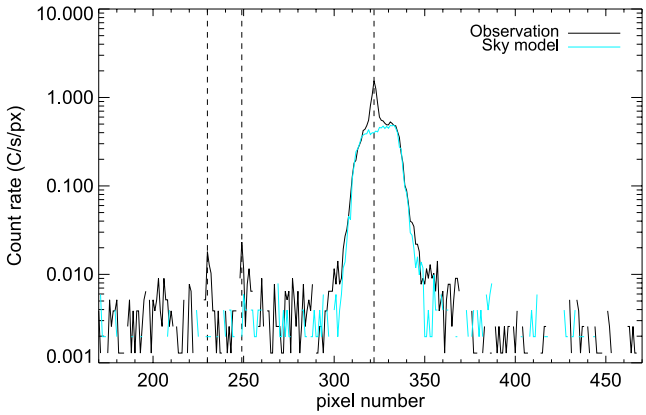

Figure 2. Example of Lyman-α emission during the Mercury's observation by the Probing the Hermean Exosphere by Ultraviolet Spectroscopy (a cut along the line 130 for observation 1 in black) and a fit of the interplanetary emission derived from sky observations (blue line). The vertical dashed lines indicate the pixel position of the observed solar emission lines at Lyman-γ, Lyman-β and Lyman-α used for wavelength calibration.

The interplanetary medium is populated by hydrogen and helium atoms able to resonantly scattered the solar He and H UV emission lines in all directions (e.g., Quémerais et al., 2013) and then in the PHEBUS FOV. The brightest signal in the images corresponds to the Lyman-α emission of the interplanetary medium (121.6 nm), which is spectrally and spatially broader than Mercury's reflected spectral component, because the interplanetary source fully covers the PHEBUS FOV, while Mercury can be considered as a point source. The other large spot near column pixel = 80 corresponds to the interplanetary emission of helium (58.4 nm). The width of the Point Spread Function (PSF) is not constant along the spectral axis (in Figure 1) and its standard deviation varies from ~1 pixel near 160 nm (column ~ 450) to ~4 pixels near 90 nm (column ~ 200) for all observations.

The Lyman-α emission of the Sun reflected by the surface of Mercury is seen on all images by the small red spot, aligned with the solar reflected spectrum, which is less extended horizontally and vertically than the interplanetary emission. While the positions of the interplanetary emission are fixed in the images, the position of the solar Lyman-α emission reflected by Mercury is shifted horizontally and vertically from one image to another. For example, on observation four it appears slightly near the center of the interplanetary emission, while for other observations it is on the left. Since the wavelength of this emission is constant (121.6 nm), the pixel—wavelength calibration of the reflected solar spectrum differs from image to image. The signature of the reflected solar spectrum is visible from column pixels ~165 to 470 (~80–160 nm). We will then consider only this spectral range. A derivation of the Mercury's albedo at 58.4 nm requires additional observations (scheduled during the rest of the cruise).

2.2. Interplanetary Medium Correction and Spectral Calibration

To isolate the reflected solar radiation at Lyman-α, we need to subtract the interplanetary Lyman-α contribution. During the cruise, few observations of the interplanetary emissions have been performed with and without the slit. Without the slit, the shape of the emission line is stable with time. Then, an interplanetary spectrum observed during the cruise, without Mercury, has been rescaled to fit the observed interplanetary emission of each observation with Mercury (Figure 2) This interplanetary emission (~0.4 count/s/px) and a dark background estimate ($\sim 2 \times 10^{-3}$ count/s/px) are subtracted from all datasets.

The rows of the detectors where the reflected solar spectrum is observed (Figure 1) are used to generate an average spectrum per observation. The number of rows added is not constant due to the nonuniformity of the PSF. The number of rows added vary from ~5 near 160 nm to ~15 rows near 90 nm. In the following section, we will call a "bin" the number of pixels in the spatial direction summed to generate the average spectrum. A bin is then a detector surface of width 1 pixel and length varying from 5 to 15 pixels.

Several emission lines are visible in the observed reflected spectrum, for example, at Lyman-α (121.6 nm), Lyman-β (102.5 nm), Lyman-γ (97.2 nm), O (130.4 nm), C^+ (133.5 nm), and Si^{3+} doublet (140 nm). These emission lines are used to calibrate the wavelengths of each spectrum. The three average spectra of each sequence (colored lines in Figure 3) are then summed to derive an average spectrum per sequence (black line in Figure 3).

The count rate of the first sequence is expected to be larger due to the closer distance of BepiColombo to Mercury (Table 1) and therefore, the final spectrum is calculated from the two average spectra weighted by the relative geometric factor Ω/D^2 (see Section 3). The final representative spectrum of the full set of observations is compared to the composite Whole Heliosphere Irradiance (WHI) solar spectrum from 25 to 29 March (Woods et al., 2009) (Figure 4) and used to derive the reflectance.

3. Results: UV Reflectance

The observed spectra presented below are not spatially resolved and correspond to disk-integrated spectra. Therefore, all the parameters studied in this manuscript correspond to disk-integrated parameters, and hereafter the term «disk-integrated» will be omitted.

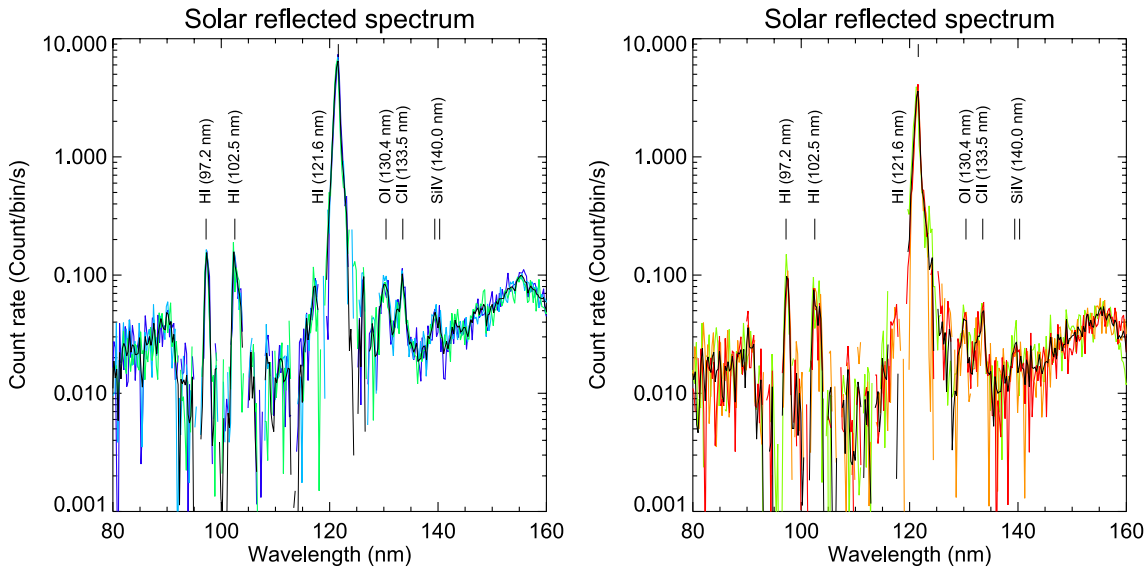

Figure 3. (Left panel) Average spectra derived for the three observations of the first sequence (colors) and the average spectrum (black). (Right panel) Average spectra for the three observations of the second sequence (colors) and the average spectrum (black). The positions of the main solar emission lines indicated by the vertical solid lines at 97.2 nm (H Lyman-γ), 102.5 nm (H Lyman-β), 121.6 nm (H Lyman-α), 130.4 nm (O I), 133.5 nm (C^+) and the doublet near 140 nm (Si^{3+}) have been used to calibrate the wavelength of each spectrum.

The disk-integrated reflectance I/F is the ratio of the radiance from the hemisphere of a planet viewed by an observer I to the radiance expected from a perfect Lambertian surface normally illuminated by the Sun F. Using the notation of Hapke (2012), we have the following equation:

$$[I/F](\lambda, g) = \frac{\int_A J(\lambda) r(i, e, g, \lambda) \frac{\mu dA}{\pi R^2}}{\frac{J(\lambda)}{\pi}} = A_p(\lambda) \Phi_p(\lambda, g) \quad (1)$$

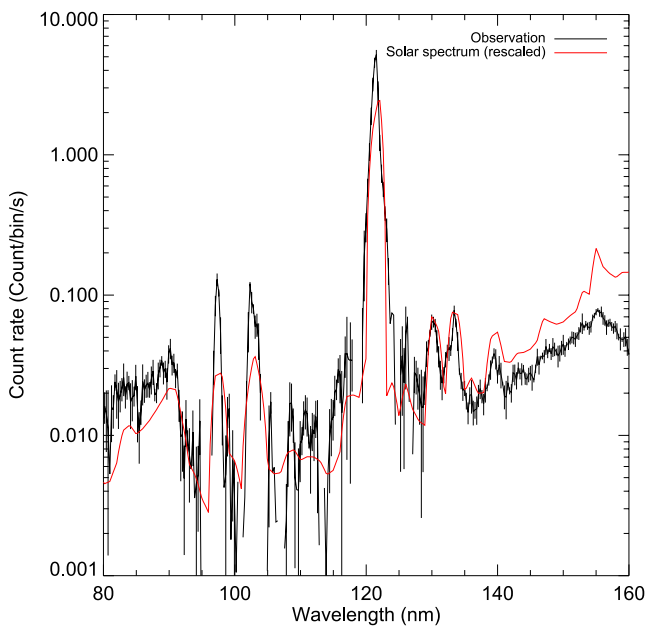

Figure 4. Average observed spectrum deduced from the full set of Probing the Hermean Exosphere by Ultraviolet Spectroscopy observations compared to the composite WHI solar spectrum arbitrarily rescaled by a constant.

where, $J(\lambda)$ is the solar spectral irradiance at the body (power per unit area per unit wavelength), $r(i, e, g, \lambda)$ is the bidirectional reflectance of the elementary surface dA (illuminated and visible by the observer) of the body at incident angle i, emission angle e ($\mu = \cos(e)$), phase angle g and wavelength λ. R is the radius of the spherical body. It can also be expressed as the product of the physical (or geometric) albedo $A_p(\lambda)$ and the integral phase function $\Phi_p(\lambda, g)$ (Hapke, 2012, Equations 11.30 and 11.35). The reflectance at $g = 0°$ is equal to the physical albedo because $\Phi_p(\lambda, 0°) = 1$.

The spectral irradiance $E_p(\lambda, g)$ at the entrance of an instrument (power per unit area) is given by the following equation:

$$E_p(\lambda, g) = \frac{\omega}{S_p} \int_A J(\lambda) r(i, e, g, \lambda) \mu d A \quad (2)$$

where ω is the solid angle of the instrument surface entrance as seen from the body and S_p is the entrance pupil of the instrument. $\omega \sim S_p/\Delta^2$, where Δ is the observer-body distance, so:

$$E_p(\lambda, g) = \frac{1}{\Delta^2} \int_A J(\lambda) r(i, e, g, \lambda) \mu d A \quad (3)$$

Then, the disk-integrated I/F can be related to E_p (Domingue et al., 2010; Holsclaw et al., 2010) by the following equation:

$$[I/F](\lambda, g) = \frac{E_p(\lambda, g) \frac{\Delta^2}{\pi R^2}}{\frac{J(\lambda)}{\pi}} = \frac{E_p(\lambda, g)}{\Omega_{object}} \frac{\pi}{J(\lambda)} \quad (4)$$

Table 2
Derived Reflectance for Several Wavelength Ranges at a Phase Angle ~70°

Spectral interval	Reflectance (in 10^{-3})	Uncertainty (random) in 10^{-4}	Uncertainty (systematic) range in 10^{-3}
Continuum 1: (87–95 nm)	3.8	2.8	2.5–4.2
H Lyman-γ: (97.2 nm)	4.2	3.0	3.5–5.5
H Lyman-β (102.5 nm)	3.7	2.4	2.5–4.2
Continuum 2 (105–115 nm)	2.2	1.9	1.7–2.5
H Lyman-α (121.6 nm)	3.5	1.4	1.9–3.8
Continuum 3 (125–128 nm)	4.3	8.6	2.9–4.7
O I (130.4 nm)	3.1	1.6	2.1–3.4
C II (133.5 nm)	2.5	0.9	1.6–2.8
Continuum 4 (135–138 nm)	2.5	1.3	1.9–2.8
Si IV (140 nm)	2.5	0.9	1.6–2.7
Continuum 5 (142–148 nm)	3.0	0.7	2.1–3.3
Continuum 6 (148–154 nm)	3.4	0.7	2.4–3.7
Continuum 7 (154–160 nm)	3.7	0.7	2.8–4.1

where $\Omega_{object} = \pi R^2/\Delta^2$ is the solid angle of the object as seen by the observer. Noting J_T the solar irradiance at 1 AU, and D the body-Sun distance (in AU), we can replace $J(\lambda) = J_T(\lambda)/D^2$ to derive the reflectance from the observation (E_p) and the solar spectrum at 1 AU J_T:

$$[I/F](\lambda, g) = \frac{E_p(\lambda, g)}{\Omega_{object}} \frac{\pi}{J_T(\lambda)} D^2 \quad (5)$$

Since it is a ratio of two spectral quantities, both E_p and J_T can be expressed either in power units (W cm^{-2} nm^{-1}) or photon units (ph s^{-1} cm^{-2} nm^{-1}).

$E_p(\lambda,g)$ is related to the count rate on the bin, CR(bin) (in counts/bin/s), derived from the full set of observations by the following equation:

$$E_p(\lambda, g) = \frac{CR(\text{bin})}{S_{eff}(\lambda)\delta\lambda} \quad (6)$$

where $S_{eff}(\lambda)$ is the effective area of the EUV channel of PHEBUS, that is, the entrance pupil area multiplied by the total efficiency of the instrument (including optics and detectors) and the vignetting inside the instrument (e.g., due to the split of the beam coming from the primary mirror on the two gratings (EUV and FUV)), and $\delta\lambda$ is the bin spectral bandpass (spectral width of one bin).

So, *I*/*F* can be deduced from the observable *CR*(bin) by

$$[I/F](\lambda, g) = \frac{1}{S_{eff}(\lambda)\delta\lambda} \frac{CR(\text{bin})}{\Omega_{object}} \frac{\pi}{J_T(\lambda)} D^2 \quad (7)$$

To avoid potential damage to the detector, the Mercury observations have been carried out with an EUV detector voltage of 3,400 V instead of the nominal 3,600 V one. A first estimate of the effective area has been derived from observations of the star α-Eridani at the same voltage above 115 nm, and β-Cani Majoris at 3,200 V above 90 nm (Appendix B). The systematic uncertainty is estimated to be 10% based on these two stars. This systematic uncertainty may include other parameters affecting the instrumental sensitivity not well estimated yet but expected to be lower than 10% (e.g., polarization,…). Below 90 nm, the starlight is strongly absorbed by the interstellar medium and the effective area has only been estimated above 90 nm.

The solar flux $J_T(\lambda)$, taken from the Whole Heliophysics Interval 2008 (https://lasp.colorado.edu/lisird/data/whi_ref_spectra), is a composite solar irradiance spectrum from 0.1 to 2,400 nm based on TIMED/SEE, SORCE and rocket experiment (Woods et al., 2009). Three spectra corresponding to three periods: 25 March–29 March, 29 March–4 April, and 10 April to 16 April 2008 are available and associated to different sunspot numbers, F10.7 index (83.8, 77.1, and 68.9), etc. Their spectral resolution varies from 0.1 nm below 105 nm and between 116–310 to 0.4 nm between 105 and 116 nm.

In October 2021, the F10.7 monthly average index, measured by the radio telescopes, located at the Dominion Radio Astrophysical Observatory (https://www.spaceweather.gc.ca/forecast-prevision/solar-solaire/solarflux/sx-en.php) was 90.5 and then the solar activity of the first period is similar to that during the PHEBUS observations, and is used here to calculate the reflectance (Table 2, column 1). However, due to the variations of the EUV solar flux with the solar activity, the solar spectrum during our observations may differ from the WHI reference spectrum A possible systematic uncertainty on the derived reflectance is considered by choosing the three periods of WHI (Woods et al., 2009) and the ATLAS-1 and ATLAS-3 spectra (Thuillier et al., 2004). We neglect the noise (random error) on these spectra because it is much smaller than the noise on the spectra measured by PHEBUS. The current systematic uncertainty on the derived reflectance is mainly instrumental (effective area), so a more accurate solar spectrum is not crucial for the first estimate presented in this manuscript, but when the effective area will be improved using future stellar observations, such details should be considered more carefully, for example, by using the measured solar spectrum from TIMED-SEE, SDO-EVE, or MAVEN-EUVM (Eparvier et al., 2015; Woods et al., 2005, 2012).

The resulting statistical uncertainty on the derived *I*/*F* is obtained from standard error propagation, while a range of values is derived from the systematic uncertainty (combining the extrema estimated for the solar spectrum and

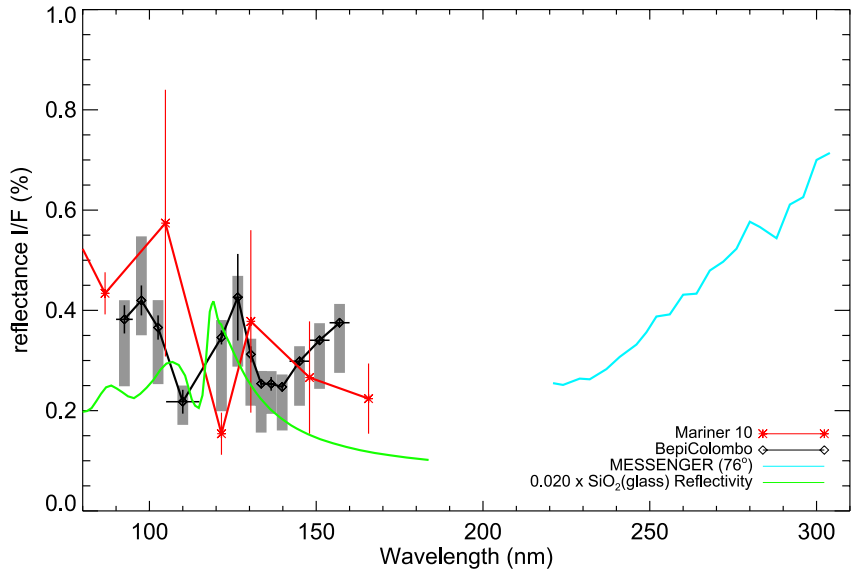

Figure 5. Spectral variation of the reflectance at a phase angle of ~70° derived from BepiColombo/PHEBUS compared to values deduced from Mariner 10 (Wu & Broadfoot, 1977), converted to reflectance at 70° (see Appendix A). The reflectance at 76° measured by MESSENGER/MASCS for wavelengths >220 nm (Holsclaw et al., 2010) is also shown. The vertical black bars represent the estimated standard deviation and the gray area represents the estimated range considering the systematic uncertainty on the solar flux and the effective area. Scaled relative reflectivity curve for SiO_2 between 80–180 nm (green curve) is plotted for comparison.

the effective area). In order to reduce the statistical uncertainty on the reflectance, especially associated to solar emission line (Figure 4), we separately estimated the reflectance at these emissions and in the different parts of the continuum. The spectral interval used to calculate the average reflectance, and the different uncertainties are given in Table 2.

The reflectance derived from the spectral range at center wavelength λ_0 is calculated from the following equation:

$$[I/F](\lambda_0, g) = \frac{\sum C(\text{bin})}{\int S_{\text{eff}}(\lambda) J_T(\lambda) \delta\lambda} \left\langle \frac{\pi D^2}{\Omega_{\text{object}}} \right\rangle \quad (8)$$

where the sum $\Sigma(CR(\text{bin}))$ is done on the bins where the emission line is observed or inside the continuum and the integral over $J_T(\lambda)S_{\text{eff}}(\lambda)\delta\lambda$ is the sum of the solar emission line of the WHI spectrum or the sum over the continuum interval. $\langle \pi D^2/\Omega_{\text{mercury}} \rangle$ is the average value for the six observations (Table 1).

The derived reflectance with their error bars and the systematic uncertainty range are compared to Mariner 10 and MESSENGER observations in Figure 5.

4. Discussion

The only measured reflectance of Mercury in the studied spectral range, before BepiColombo observations, are those from Mariner 10 during the three flybys of Mercury (Wu & Broadfoot, 1977). The observations were done at a phase angle varying from 106° incoming to 74° outgoing during flybys 1 and 3 and from 50° to 120° during the second encounter (Wu & Broadfoot, 1977). The measured reflectance at each phase angle was normalized to 0° phase angle (geometric albedo) using the integral phase function $\Phi_p(g)$ from Hapke (1966), including the Shadow-Hiding Opposite Effect (SHOE), and a value of 0.6 for the h parameter for all wavelengths (Wu & Broadfoot, 1977). Using a similar model (see appendix A), we estimate the value of $\Phi_p(70°) = 0.14$, applied it (Equation 1) to convert the geometric albedos measured by Mariner 10 into reflectance at 70°, assuming the spectral variation of this phase function to be small and therefore negligible. The magnitudes of the reflectance measured by BepiColombo/PHEBUS and Mariner 10 (between 0.1% and 0.6%) are of the same order (Figure 5). MESSENGER measured the reflectance of the surface of Mercury at wavelengths >220 nm for a phase angle $g = 76°$ (see Figures 6 and 9 from Holsclaw et al., 2010), similar to the PHEBUS observations.

The spectral variations, considering the systematic uncertainties, measured by PHEBUS display a possible local minimum between 105 and 115 nm and a local maximum between 125 and 128 nm. These maximum and minimum points are not seen at these wavelengths in Mariner's 10 observations (Figure 5) which indicate a noisy decrease of the albedo from 100 to 165.7 nm, similar to that seen on the Moon (Gladstone et al., 1994; Hendrix, Retherford, et al., 2012; Lucke et al., 1976). SiO_2 reflectance was suggested to explain partly the spectral variations on the Moon between 50 and 120 nm (Flynn et al., 1998; Gladstone et al., 1994). Its reflectance presents a local minimum of reflectivity at 115 nm and a local maximum at 120 nm (Philipp, 1985), which could explain the shape of the derived spectral profile between 110–140 nm (Figure 5).

With $\Phi_p(70°) = 0.14$, the physical albedo $A_p(\lambda)$ is between 1% and 4%, lower than the physical albedo of the Moon ~2%–8% (Gladstone et al., 1994; Wu & Broadfoot, 1977), and consistent with a lower FeO concentration on Mercury than on the Moon (Domingue et al., 2014; Hapke, 1977; Murchie et al., 2018 and references therein). This reduced FeO concentration could be due to a larger space weathering of the surface of Mercury.

The surface of airless bodies such as the Moon, Mercury, asteroids, Jovian, or Saturnian satellites is known to be subject to such space weathering processes (Pieters & Noble, 2016). The variations of the optical properties due to space weathering depend on the composition of the surface (e.g., Hendrix, Domingue, & Noll, 2012) but also on the wavelength. For example, it is well-established that the visible and near-infrared reflectance of surfaces bombarded by energetic plasma or micrometeoroids is darker and redder due to the formation of submicroscopic iron phases (SMFe) (Hapke, 2001). Space weathering and the formation of SMFe have been inferred on Mercury from infrared observations (Hapke, 1977, 2001; Lucey & Riner, 2011; Rava & Hapke, 1987; Vilas, 1988). At Mercury, impact vapor deposits are more important than on the Moon (Cintala, 1992) and the interpretation of the Mariner 10 observations suggested that Mercury had a crust with low abundance in ferrous iron (iron (II) like FeO). Hapke (2001) discuss the possibility that almost all FeO could have been converted into SMFe by space weathering on Mercury but rejected this explanation based on theoretical studies, suggesting a SMFe fraction lower than 1% and therefore inconsistent with this explanation (see also Warell & Valegard, 2006). More recent estimates of the SMFe fraction suggest a fraction of SMFe lower than the Moon (<0.5%) (McClintock et al., 2008). However, Lucey and Riner (2011) using a model with different sizes of SMFe were able to reproduce the near-infrared MASCS data with a fraction of 3.5% much larger than the lunar soils, suggesting that a major fraction of the available iron has been processed into submicroscopic iron by space weathering. A limitation of their model was the impossibility to reproduce the observed oxygen-metal charge transfer band observed by MASCS (McClintock et al., 2008).

However, the decrease of the reflectance measured by MESSENGER/MASCS from 1% at 400 nm to 0.25% at 220 nm, close to the value derived from PHEBUS below 160 nm (Figure 5), is more consistent with slopes measured on crushed lunar rocks (from ~0.2 to 0.05) than lunar soils (from 0.08 to 0.04) in contradiction with a larger space-weathering of the surface of Mercury (Hendrix & Vilas, 2006). On the contrary, the upturn of the reflectance below 200 nm is more consistent with the lunar soils (Hendrix & Vilas, 2006). If we assume an integral phase function $\Phi_p(70°) = 0.14$, the physical albedo A_p (called absolute reflectance by Hendrix & Vilas, 2006) deduced from Equation 1, decreases from 7% at 400 nm to 2% near 160 nm, which is darker than the physical albedo of crushed lunar rocks by a factor of ~2 (Hendrix & Vilas, 2006). Therefore, UV albedo of Mercury and its spectral variation can't be explained only by the space-weathering effects on the iron at the surface.

Other opaque materials such as carbonaceous materials delivered by micrometeorites (Syal et al., 2015) or the remnants of an ancient graphite-rich crust (Peplowski et al., 2016), present in the darkest terrains of Mercury (Trang et al., 2017), and their UV refractive index measurements (e.g., Applin et al., 2018) will be useful to further interpret these PHEBUS observations in the future.

5. Conclusion

Nine days after the first flyby of Mercury by the ESA-JAXA mission BepiColombo, the EUV spectrograph of PHEBUS observed the disk-integrated solar reflected light from the surface of Mercury between 90 and 160 nm at a distance of 4.5 million kilometers. From these observations, we derived the UV reflectance (between 80 and 160 nm) of Mercury's surface more than 40 years after the only measurement done before by Mariner 10. The magnitude of the reflectance measured at a phase angle of 70° is in good agreement with the Mariner 10 observations and with the MESSENGER/MASCS observations at 220 nm. The results confirm a lower EUV

albedo of Mercury compared with the Moon, probably due to a lower FeO concentration, and a possible signature of amorphous SiO_2 that needs to be confirmed by future observations. A number of favorable geometries to observe Mercury during the rest of the cruise exist, but the spacecraft operations could reduce this number (e.g., the observations were not possible after the second flyby due to spacecraft operations). After the insertion around Mercury, the reflected light from the dayside surface of Mercury will be too bright for the instrument to be observed. Therefore, the cruise observations of Mercury from a large distance are the only opportunities to better characterize the UV spectral variations of the reflectance of the surface of Mercury.

Appendix A: Integral Phase Function

To compare our derived reflectance near 70° to the published physical albedo derived from Mariner 10, we have used the model of the integral phase function given by Wu and Broadfoot (1977). This model is from Hapke (1966) and, even if such a model has been refined later (Hapke, 2012), this old version has to be used to compare with Mariner 10 published disk-integrated reflectance because they were normalized to 0° and the unprocessed values are not available. In this model, the integral phase function is the product of three terms (Hapke, 1966, Equation 9):

$$\Phi_p(g) = I(g)\Sigma(g)B(g) \tag{A1}$$

$B(g)$ is the retrodirective function which describes the backscattering due to blocking and shadowing effects within the lunar soil and depends on a parameter h which defines the sharpness of the brightness near $g = 0°$.

$$B(g) = \begin{cases} 2 - \frac{\tan(g)}{2h}(1 - \exp[-h/\tan(g)])(3 - \exp[-h/\tan(g)]) & g<\pi/2 \\ 1 & g>\pi/2 \end{cases} \tag{A2}$$

$\Sigma(g)$ describes the average angular scattering function of a single particle of the lunar soil and is the sum of the scattering function of a sphere, each of whose elements reflect the light according to the Lambert's law (Schoenberg function) and an empirical forward scattering term describing the light transmitted through the particle.

$$\Sigma(g) = \frac{\sin(g) + (\pi - g)\cos(g)}{\pi} + 0.1[1 - \cos(g)]^2 \tag{A3}$$

and $I(g)$ is the integral of the reflection function of a surface whose reflectance obeys to the Lommel-Seeliger law, over the part of the Hermean sphere that is both visible and illuminated. $I(g)$ is given by Equation A4 (Hapke, 1963, 1966)

$$I(g) = \frac{1}{2}\left(1 + \sin\left(\frac{g}{2}\right)\tan\left(\frac{g}{2}\right)\ln\left[\tan\left(\frac{g}{4}\right)\right]\right) \tag{A4}$$

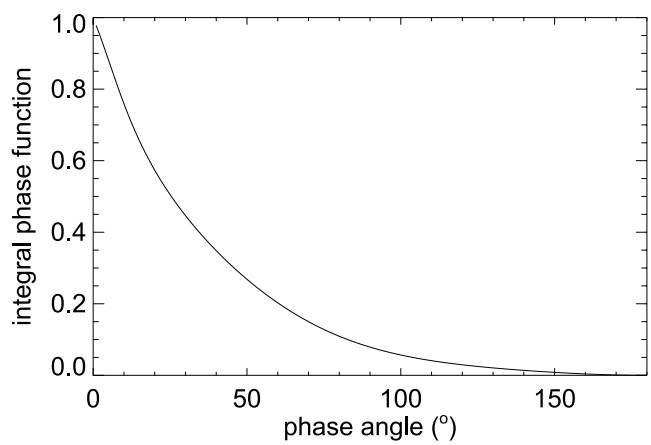

Figure A1. Integral phase function derived from the Hapke (1966) model with a parameter $h = 0.6$.

The function $\Phi_p(g)$ for $h = 0.6$ (Wu & Broadfoot, 1977) is shown in Figure A1.

Appendix B: EUV Effective Area

The EUV effective area was derived from α-Eridani observation at 3,400 V above 115 nm and from β Cani-Majoris at 3,200 V above 90 nm (Figure B1) and their measured count rate is given in Tables B1 and B2. These two observations were performed during the cruise. A shift in the wavelength given in these tables is applied to match the absorption lines in the reference spectra. The reference spectra are those of the catalog Fully ON-line Datacenter for Ultraviolet Emissions (FONDUE) (Snow et al., 2013). The effective area derived from β Cani-Majoris is rescaled to consider the difference in high voltage, and smoothed to remove the spectral featured to derive the effective area of PHEBUS (Figure B1). From the differences between the effective area derived with the two stars, we consider a possible systematic uncertainty of 10%.

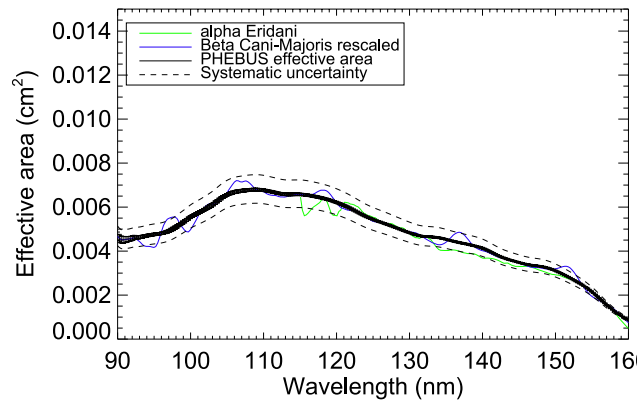

Figure B1. Effective area of Probing the Hermean Exosphere by Ultraviolet Spectroscopy (solid black line). The effective area between 115 and 160 nm derived from α-Eridani at HV = 3,400 V is shown in green, and the effective area between 90 and 160 nm derived from β Cani-Majoris at HV = 3,200 V and rescaled to take into account the difference in HV is shown in blue. The solid black dashed lines bracket the considered systematic uncertainty.

Table B1
Count Rate Measured for α-Eridani and Its Uncertainty for a Total Integration Time of 480 s

Pixel wavelength (nm)	Count rate (counts/s)	Uncertainty (counts/s)
80.0810	0.152448	0.0233854
80.3440	0.179993	0.0235702
80.6070	0.221660	0.0253448
80.8700	0.160081	0.0230112
81.1330	0.167251	0.0236621
81.3960	0.165060	0.0225347
81.6590	0.173919	0.0234780
81.9220	0.171463	0.0232924
82.1850	0.183415	0.0235702
82.4480	0.209380	0.0244736
82.7110	0.174709	0.0231053
82.9740	0.149906	0.0218502
83.2370	0.218481	0.0247382
83.5000	0.225346	0.0244736
83.7630	0.188592	0.0230112
84.0260	0.185565	0.0228218

Table B1
Continued

Pixel wavelength (nm)	Count rate (counts/s)	Uncertainty (counts/s)
84.2890	0.168481	0.0225347
84.5520	0.225719	0.0245621
84.8150	0.190675	0.0231053
85.0780	0.192561	0.0232924
85.3410	0.161706	0.0216506
85.6040	0.158702	0.0211435
85.8670	0.217605	0.0238448
86.1300	0.206619	0.0233854
86.3930	0.213089	0.0232924
86.6560	0.217058	0.0235702
86.9190	0.211926	0.0235702
87.1820	0.192803	0.0226308
87.4450	0.207189	0.0233854
87.7080	0.214799	0.0232924
87.9710	0.206026	0.0236621
88.2340	0.173855	0.0218502
88.4970	0.221072	0.0232924
88.7600	0.196970	0.0228218
89.0230	0.222190	0.0235702
89.2860	0.213636	0.0235702
89.5490	0.225171	0.0242956
89.8120	0.268176	0.0259373
90.0750	0.237298	0.0247382
90.3380	0.263636	0.0256851
90.6010	0.203022	0.0231990
90.8640	0.256816	0.0254303
91.1270	0.177057	0.0222439
91.3900	0.253417	0.0251730
91.6530	0.291663	0.0268419
91.9160	0.217255	0.0234780
92.1790	0.241618	0.0253448
92.4420	0.285193	0.0269226
92.7050	0.282714	0.0270031
92.9680	0.366815	0.0299739
93.2310	0.441290	0.0320725
93.4940	0.473263	0.0333984
93.7570	0.574008	0.0365029
94.0200	0.666268	0.0388641
94.2830	0.898240	0.0448764
94.5460	1.37778	0.0549226
94.8090	1.65826	0.0600564
95.0720	2.09730	0.0671532
95.3350	3.99197	0.0920447

Table *B1*
Continued

Pixel wavelength (nm)	Count rate (counts/s)	Uncertainty (counts/s)
95.5980	5.59067	0.108553
95.8610	4.88820	0.101636
96.1240	3.36793	0.0846254
96.3870	3.75980	0.0892922
96.6500	8.03649	0.129971
96.9130	14.1827	0.172338
97.1760	16.5776	0.186211
97.4390	16.4922	0.185732
97.7020	15.6263	0.180794
97.9650	12.9501	0.164702
98.2280	7.72624	0.127493
98.4910	3.33738	0.0844457
98.7540	2.15124	0.0681158
99.0170	3.81616	0.0902110
99.2800	8.14019	0.130985
99.5430	12.4610	0.161777
99.8060	13.1180	0.165936
100.069	10.7409	0.150275
100.332	9.96784	0.144788
100.595	10.8510	0.151024
100.858	13.7340	0.169699
101.121	18.8790	0.198836
101.384	23.5847	0.222127
101.647	25.3549	0.230310
101.910	24.9089	0.228294
102.173	23.4547	0.221589
102.436	22.2596	0.215944
102.699	25.2852	0.229989
102.962	23.7407	0.222897
103.225	20.6202	0.207843
103.488	13.7151	0.169737
103.751	6.19126	0.114602
104.014	3.32477	0.0846767
104.277	6.65185	0.118750
104.540	12.2008	0.160037
104.803	13.6699	0.169456
105.066	11.3604	0.154659
105.329	20.1301	0.205280
105.592	32.3534	0.260016
105.855	38.4848	0.283448
106.118	39.2667	0.286366
106.381	37.3673	0.279322
106.644	36.4620	0.275906

Table *B1*
Continued

Pixel wavelength (nm)	Count rate (counts/s)	Uncertainty (counts/s)
106.907	34.4385	0.268160
107.170	34.1594	0.267098
107.433	35.4208	0.271929
107.696	32.7935	0.261631
107.959	30.9335	0.254124
108.222	31.6844	0.257264
108.485	34.5128	0.268435
108.748	34.0160	0.266545
109.011	34.7441	0.269331
109.274	36.9672	0.277764
109.537	35.9120	0.273845
109.800	28.8739	0.245621
110.063	26.6497	0.236015
110.326	31.6192	0.257003
110.589	33.1531	0.263119
110.852	34.8989	0.269991
111.115	34.7955	0.269556
111.378	34.5404	0.268564
111.641	35.8010	0.273401
111.904	36.2319	0.275032
112.167	31.9799	0.258518
112.430	27.0413	0.237765
112.693	27.6258	0.240307
112.956	31.3924	0.256165
113.219	34.4669	0.268354
113.482	33.1289	0.263177
113.745	31.2598	0.255640
114.008	29.1593	0.246934
114.271	27.3534	0.239148
114.534	29.6710	0.249069
114.797	33.0799	0.262963
115.060	33.8566	0.266039
115.323	32.4019	0.260400
115.586	31.0308	0.254942
115.849	31.3153	0.256292
116.112	32.1778	0.260016
116.375	34.8694	0.271234
116.638	35.4915	0.274542
116.901	34.4285	0.272001
117.164	34.8160	0.277099
117.427	35.5135	0.285622
117.690	35.5812	0.292647
117.953	35.7446	0.298739

Table *B1*
Continued

Pixel wavelength (nm)	Count rate (counts/s)	Uncertainty (counts/s)
118.216	34.5260	0.299261
118.479	33.6930	0.298506
118.742	32.0562	0.294966
119.005	29.4979	0.287885
119.268	28.9305	0.286971
119.531	32.4666	0.301465
119.794	33.3643	0.305299
120.057	33.5241	0.307685
120.320	31.1026	0.300571
120.583	29.0213	0.294488
120.846	27.6111	0.290743
121.109	25.6612	0.285097
121.372	24.5348	0.282013
121.635	20.6061	0.268022
121.898	16.2416	0.251730
122.161	11.8253	0.233287
122.424	9.96845	0.225568
122.687	9.03385	0.222127
122.950	9.42838	0.223199
123.213	9.79414	0.223859
123.476	12.4620	0.233296
123.739	16.8635	0.249113
124.002	19.2072	0.253200
124.265	22.4596	0.259147
124.528	25.0561	0.259908
124.791	26.1558	0.254389
125.054	28.8422	0.257467
125.317	30.2708	0.259423
125.580	31.3061	0.261954
125.843	32.4917	0.265443
126.106	32.8073	0.265525
126.369	32.5302	0.263581
126.632	32.3546	0.262318
126.895	32.0836	0.260841
127.158	32.5538	0.262144
127.421	32.0983	0.260075
127.684	31.8000	0.258703
127.947	30.5245	0.253217
128.210	30.3786	0.252470
128.473	30.9300	0.254644
128.736	32.1466	0.259457
128.999	32.1544	0.259415
129.262	31.9177	0.258401

Table *B1*
Continued

Pixel wavelength (nm)	Count rate (counts/s)	Uncertainty (counts/s)
129.525	31.1763	0.255359
129.788	31.1704	0.255291
130.051	31.7672	0.257694
130.314	31.0697	0.254866
130.577	30.2173	0.251299
130.840	28.6226	0.244568
131.103	27.3342	0.238985
131.366	25.6586	0.231541
131.629	25.1823	0.229403
131.892	24.5734	0.226595
132.155	24.4723	0.226135
132.418	25.6770	0.231644
132.681	25.5310	0.230940
132.944	26.0308	0.233250
133.207	27.6590	0.240406
133.470	28.0537	0.242035
133.733	27.9653	0.241676
133.996	27.5219	0.239764
134.259	27.5751	0.239991
134.522	26.7331	0.236300
134.785	26.4551	0.235066
135.048	25.2781	0.229866
135.311	24.5658	0.226576
135.574	24.5817	0.226662
135.837	25.1891	0.229432
136.100	25.7496	0.231934
136.363	26.3681	0.234706
136.626	25.8928	0.232551
136.889	26.0907	0.233436
137.152	25.6778	0.231578
137.415	25.8058	0.232215
137.678	25.5467	0.231034
137.941	25.6606	0.231503
138.204	24.8821	0.228018
138.467	24.6528	0.226978
138.730	24.7034	0.227150
138.993	24.6115	0.226710
139.256	23.9818	0.223830
139.519	23.8782	0.223345
139.782	23.1926	0.220135
140.045	23.2060	0.220233
140.308	22.8322	0.218393
140.571	22.8479	0.218462

Table *B1*
Continued

Pixel wavelength (nm)	Count rate (counts/s)	Uncertainty (counts/s)
140.834	22.6369	0.217516
141.097	21.6471	0.212765
141.360	21.3085	0.211014
141.623	21.6846	0.212918
141.886	21.6882	0.212908
142.149	21.7357	0.213132
142.412	21.7981	0.213417
142.675	21.9107	0.213986
142.938	21.8795	0.213773
143.201	21.9163	0.213966
143.464	21.9973	0.214401
143.727	21.4803	0.211835
143.990	21.4920	0.211938
144.253	21.2590	0.210798
144.516	21.3648	0.211261
144.779	21.6113	0.212490
145.042	21.2559	0.210695
145.305	21.1505	0.210210
145.568	21.3034	0.210983
145.831	20.8515	0.208729
146.094	21.2935	0.210963
146.357	20.9958	0.209476
146.620	21.1528	0.210241
146.883	21.0248	0.209569
147.146	21.0549	0.209756
147.409	20.8331	0.208614
147.672	20.7072	0.208010
147.935	20.5191	0.207038
148.198	20.6672	0.207833
148.461	20.1485	0.205185
148.724	19.9966	0.204369
148.987	19.7430	0.203101
149.250	19.9564	0.204230
149.513	19.6055	0.202362
149.776	19.3464	0.201071
150.039	18.9604	0.199097
150.302	18.5771	0.197015
150.565	18.1918	0.194989
150.828	17.6926	0.192322
151.091	18.1295	0.194644
151.354	18.0311	0.194086
151.617	17.6341	0.192017
151.880	17.4712	0.191088

Table *B1*
Continued

Pixel wavelength (nm)	Count rate (counts/s)	Uncertainty (counts/s)
152.143	17.2892	0.190109
152.406	16.5500	0.185989
152.669	16.8333	0.187604
152.932	16.2812	0.184478
153.195	16.1248	0.183570
153.458	16.0229	0.182978
153.721	15.3848	0.179348
153.984	15.2546	0.178560
154.247	15.1566	0.177988
154.510	14.7422	0.175570
154.773	14.6315	0.174864
155.036	14.0745	0.171493
155.299	13.6261	0.168814
155.562	13.1714	0.165949
155.825	12.8803	0.164068
156.088	12.4809	0.161509
156.351	12.4347	0.161280
156.614	12.3184	0.160498
156.877	12.0544	0.158689
157.140	11.6396	0.156042
157.403	11.1379	0.152582
157.666	10.8069	0.150289
157.929	10.8925	0.150952
158.192	10.3398	0.147004
158.455	10.0728	0.145177
158.718	9.92204	0.144021
158.981	9.47355	0.140745
159.244	8.88019	0.136247
159.507	8.47243	0.133089
159.770	8.09574	0.130071
160.033	7.74252	0.127220
160.296	7.00846	0.120977
160.559	6.71943	0.118512
160.822	6.34254	0.115131
161.085	5.54447	0.107569
161.348	4.18691	0.0934718
161.611	3.74561	0.0884374
161.874	3.09239	0.0803908
162.137	2.56210	0.0731247
162.400	2.21873	0.0680839
162.663	2.02706	0.0650854
162.926	1.82289	0.0617314
163.189	1.75548	0.0605243

Table *B1*
Continued

Pixel wavelength (nm)	Count rate (counts/s)	Uncertainty (counts/s)
163.452	1.51741	0.0562886
163.715	1.31855	0.0524570
163.978	1.21230	0.0503029
164.241	1.12346	0.0485019
164.504	0.981052	0.0452616
164.767	0.880285	0.0429490
165.030	0.853026	0.0421843
165.293	0.735219	0.0391977
165.556	0.705110	0.0383582
165.819	0.612873	0.0357824
166.082	0.593552	0.0352324
166.345	0.576886	0.0347361
166.608	0.520263	0.0329404
166.871	0.413245	0.0294628
167.134	0.423289	0.0297560
167.397	0.338443	0.0265982
167.660	0.325943	0.0261041
167.923	0.348860	0.0270031
168.186	0.262500	0.0233854
168.449	0.318750	0.0257694
168.712	0.289583	0.0245621
168.975	0.288443	0.0245621
169.238	0.322346	0.0259373
169.501	0.255110	0.0231053
169.764	0.303026	0.0251730
170.027	0.322346	0.0259373
170.290	0.322346	0.0259373

Table B2
Count Rate Measured for β Cani-Majoris and Its Uncertainty for a Total Integration Time of 480 s

Pixel wavelength (nm)	Count rate (counts/s)	Uncertainty (counts/s)
80.0810	0.207450	0.0218502
80.3440	0.309469	0.0261041
80.6070	0.319885	0.0265165
80.8700	0.286617	0.0253448
81.1330	0.326353	0.0270031
81.3960	0.310104	0.0261871
81.6590	0.340236	0.0273227
81.9220	0.322845	0.0266797
82.1850	0.340719	0.0273227
82.4480	0.326377	0.0267609
82.7110	0.334622	0.0271633

Table *B2*
Continued

Pixel wavelength (nm)	Count rate (counts/s)	Uncertainty (counts/s)
82.9740	0.397057	0.0293151
83.2370	0.341925	0.0273227
83.5000	0.446115	0.0308305
83.7630	0.427277	0.0302622
84.0260	0.409798	0.0297560
84.2890	0.434469	0.0306894
84.5520	0.452913	0.0311805
84.8150	0.552913	0.0343592
85.0780	0.492496	0.0324760
85.3410	0.573746	0.0349851
85.6040	0.527913	0.0335927
85.8670	0.590413	0.0354779
86.1300	0.579119	0.0351090
86.3930	0.539865	0.0338502
86.6560	0.608133	0.0359035
86.9190	0.719668	0.0390312
87.1820	0.743461	0.0396928
87.4450	0.688812	0.0382449
87.7080	0.860369	0.0426448
87.9710	0.868614	0.0428985
88.2340	0.872210	0.0430500
88.4970	0.845721	0.0421843
88.7600	1.02936	0.0465848
89.0230	0.984822	0.0455007
89.2860	1.04313	0.0469560
89.5490	1.14802	0.0492125
89.8120	1.25204	0.0513279
90.0750	1.33857	0.0530739
90.3380	1.46429	0.0554730
90.6010	1.66125	0.0590727
90.8640	1.94201	0.0638398
91.1270	2.46173	0.0718070
91.3900	3.00508	0.0792762
91.6530	3.70949	0.0880439
91.9160	4.64316	0.0984471
92.1790	5.75059	0.109588
92.4420	6.69114	0.118182
92.7050	8.51548	0.133333
92.9680	9.88633	0.143599
93.2310	10.8785	0.150621
93.4940	11.8022	0.156901
93.7570	13.5202	0.167925
94.0200	14.3951	0.173255

Table *B2*
Continued

Pixel wavelength (nm)	Count rate (counts/s)	Uncertainty (counts/s)
94.2830	14.1491	0.171783
94.5460	14.0191	0.171024
94.8090	14.9100	0.176347
95.0720	16.3043	0.184384
95.3350	17.1000	0.188838
95.5980	17.5050	0.191043
95.8610	17.4376	0.190679
96.1240	17.1420	0.189056
96.3870	16.5653	0.185861
96.6500	15.2321	0.178244
96.9130	13.0265	0.164834
97.1760	10.5910	0.148648
97.4390	9.09842	0.137800
97.7020	8.63103	0.134226
97.9650	10.3757	0.147137
98.2280	12.2668	0.159983
98.4910	13.1883	0.165884
98.7540	13.0751	0.165136
99.0170	12.4840	0.161428
99.2800	12.8478	0.163724
99.5430	14.2184	0.172263
99.8060	16.6013	0.186083
100.069	17.9994	0.193750
100.332	18.2776	0.195256
100.595	18.1605	0.194622
100.858	17.4898	0.190986
101.121	17.8401	0.192897
101.384	16.7893	0.187152
101.647	16.4539	0.185276
101.910	15.5299	0.180037
102.173	14.9339	0.176543
102.436	13.8722	0.170184
102.699	12.7518	0.163140
102.962	13.6034	0.168493
103.225	14.3942	0.173343
103.488	14.6022	0.174565
103.751	15.7661	0.181382
104.014	18.2788	0.195278
104.277	21.0928	0.209766
104.540	22.9687	0.218839
104.803	23.3357	0.220617
105.066	23.4639	0.221226
105.329	23.6954	0.222283

Table *B2*
Continued

Pixel wavelength (nm)	Count rate (counts/s)	Uncertainty (counts/s)
105.592	23.2014	0.219957
105.855	22.8810	0.218412
106.118	22.0345	0.214361
106.381	21.7028	0.212745
106.644	21.9356	0.213864
106.907	22.9949	0.218958
107.170	23.0520	0.219236
107.433	23.4044	0.220892
107.696	24.7854	0.227313
107.959	25.9950	0.232784
108.222	26.2914	0.234123
108.485	24.8347	0.227542
108.748	23.5543	0.221608
109.011	24.4616	0.225818
109.274	26.1501	0.233473
109.537	27.1672	0.237993
109.800	27.8112	0.240776
110.063	28.4839	0.243688
110.326	29.1123	0.246345
110.589	29.5316	0.248127
110.852	28.6140	0.244239
111.115	28.3094	0.242938
111.378	28.2934	0.242867
111.641	28.9226	0.245551
111.904	29.2160	0.246785
112.167	28.3764	0.243233
112.430	27.6308	0.240027
112.693	26.8113	0.236447
112.956	26.9252	0.236942
113.219	27.7779	0.240677
113.482	29.9195	0.249774
113.745	30.5928	0.252556
114.008	30.9086	0.253868
114.271	31.4893	0.256225
114.534	31.3761	0.255767
114.797	32.0553	0.258518
115.060	32.6899	0.261074
115.323	33.2121	0.263169
115.586	33.2636	0.263391
115.849	33.5271	0.264485
116.112	33.2652	0.263531
116.375	33.2363	0.263573
116.638	33.7254	0.265745

Table *B2*
Continued

Pixel wavelength (nm)	Count rate (counts/s)	Uncertainty (counts/s)
116.901	33.1648	0.263935
117.164	31.6181	0.258719
117.427	31.1741	0.258535
117.690	31.0759	0.259950
117.953	29.9600	0.257011
118.216	30.6643	0.261132
118.479	32.0035	0.266927
118.742	33.1398	0.271937
119.005	34.0003	0.275741
119.268	33.8673	0.275575
119.531	33.6674	0.275260
119.794	33.0670	0.273322
120.057	32.7819	0.272614
120.320	31.5744	0.268370
120.583	31.0050	0.266365
120.846	30.2650	0.263861
121.109	29.1513	0.259791
121.372	29.4347	0.261240
121.635	30.2591	0.264633
121.898	30.2996	0.265124
122.161	30.4446	0.265803
122.424	31.0392	0.268330
122.687	33.2232	0.276762
122.950	35.0771	0.283509
123.213	35.4639	0.284663
123.476	36.0431	0.286191
123.739	36.7469	0.288013
124.002	37.0554	0.287915
124.265	37.9284	0.289418
124.528	38.3760	0.288825
124.791	38.6126	0.287643
125.054	39.0479	0.287681
125.317	39.2404	0.287545
125.580	38.6735	0.285188
125.843	39.1173	0.286532
126.106	39.5793	0.287968
126.369	39.2826	0.286721
126.632	39.0916	0.285903
126.895	39.5913	0.287621
127.158	40.1633	0.289583
127.421	40.0324	0.289081
127.684	40.0555	0.289126
127.947	40.2613	0.289808

Table *B2*
Continued

Pixel wavelength (nm)	Count rate (counts/s)	Uncertainty (counts/s)
128.210	39.9547	0.288668
128.473	40.1512	0.289381
128.736	39.2745	0.286176
128.999	38.7137	0.284113
129.262	38.2597	0.282436
129.525	38.3986	0.282942
129.788	38.2908	0.282520
130.051	38.4886	0.283257
130.314	38.1695	0.282090
130.577	37.7146	0.280392
130.840	37.1462	0.278263
131.103	37.0567	0.277920
131.366	37.3184	0.278902
131.629	37.1310	0.278193
131.892	37.0457	0.277865
132.155	37.0089	0.277748
132.418	37.7173	0.280384
132.681	37.6401	0.280090
132.944	36.9463	0.277522
133.207	36.8136	0.277005
133.470	36.5452	0.275985
133.733	35.7134	0.272837
133.996	35.3266	0.271354
134.259	34.9507	0.269910
134.522	34.8165	0.269379
134.785	34.6044	0.268564
135.048	34.8048	0.269347
135.311	35.1335	0.270617
135.574	34.2635	0.267252
135.837	34.2029	0.267016
136.100	33.3940	0.263828
136.363	33.8015	0.265427
136.626	33.1160	0.262731
136.889	33.4241	0.263951
137.152	32.4206	0.259958
137.415	31.4065	0.255860
137.678	31.8591	0.257711
137.941	31.0151	0.254261
138.204	30.3713	0.251609
138.467	30.3664	0.251592
138.730	29.9338	0.249792
138.993	29.6667	0.248677
139.256	30.0453	0.250243

Table *B2*
Continued

Pixel wavelength (nm)	Count rate (counts/s)	Uncertainty (counts/s)
139.519	29.5204	0.248065
139.782	29.3669	0.247417
140.045	28.6700	0.244488
140.308	27.9685	0.241460
140.571	27.1132	0.237747
140.834	26.7628	0.236199
141.097	26.8773	0.236713
141.360	26.5081	0.235075
141.623	25.9946	0.232803
141.886	26.1937	0.233686
142.149	26.2267	0.233816
142.412	26.8741	0.236685
142.675	26.3002	0.234160
142.938	26.4709	0.234900
143.201	26.3575	0.234400
143.464	26.2728	0.234021
143.727	26.1912	0.233668
143.990	26.0696	0.233129
144.253	25.7678	0.231775
144.516	25.6715	0.231316
144.779	25.7089	0.231494
145.042	25.1490	0.228958
145.305	25.4033	0.230121
145.568	24.7906	0.227332
145.831	25.0347	0.228455
146.094	24.7794	0.227284
146.357	24.7594	0.227179
146.620	24.5649	0.226289
146.883	24.3844	0.225453
147.146	24.2915	0.225029
147.409	23.9793	0.223578
147.672	23.3838	0.220794
147.935	23.3967	0.220843
148.198	22.8094	0.218084
148.461	22.8387	0.218204
148.724	22.6291	0.217187
148.987	22.0332	0.214320
149.250	21.6257	0.212347
149.513	21.6256	0.212326
149.776	21.5801	0.212112
150.039	21.0785	0.209642
150.302	20.5750	0.207101

Table *B2*
Continued

Pixel wavelength (nm)	Count rate (counts/s)	Uncertainty (counts/s)
150.565	20.5636	0.207048
150.828	19.7830	0.203090
151.091	20.0665	0.204538
151.354	19.8784	0.203571
151.617	19.7496	0.202919
151.880	18.9932	0.198988
152.143	18.5329	0.196585
152.406	17.8334	0.192829
152.669	17.7452	0.192356
152.932	17.3059	0.189961
153.195	17.2361	0.189560
153.458	16.4726	0.185323
153.721	16.6061	0.186083
153.984	16.2118	0.183842
154.247	15.8507	0.181788
154.510	15.7225	0.181046
154.773	15.0030	0.176863
155.036	14.5081	0.173918
155.299	14.0801	0.171341
155.562	13.8134	0.169712
155.825	13.3901	0.167083
156.088	13.2528	0.166236
156.351	12.1416	0.159126
156.614	11.6134	0.155624
156.877	11.3728	0.153984
157.140	10.9431	0.151067
157.403	10.4662	0.147741
157.666	10.0906	0.145057
157.929	9.92039	0.143841
158.192	9.61520	0.141590
158.455	9.65493	0.141896
158.718	9.60870	0.141544
158.981	9.06103	0.137453
159.244	8.95982	0.136693
159.507	8.74164	0.134999
159.770	8.61088	0.133983
160.033	8.30991	0.131630
160.296	7.85055	0.127917
160.559	7.58748	0.125779
160.822	7.27506	0.123146
161.085	7.25824	0.122987
161.348	6.45296	0.115958

Table *B2*
Continued

Pixel wavelength (nm)	Count rate (counts/s)	Uncertainty (counts/s)
161.611	6.01842	0.111997
161.874	5.52932	0.107347
162.137	4.93397	0.101401
162.400	4.63445	0.0982706
162.663	4.30224	0.0946943
162.926	4.00112	0.0913109
163.189	3.76594	0.0885845
163.452	3.38862	0.0840335
163.715	3.27268	0.0825747
163.978	3.17219	0.0813034
164.241	2.91522	0.0779512
164.504	2.79118	0.0762625
164.767	2.71778	0.0752600
165.030	2.57684	0.0732729
165.293	2.47660	0.0718372
165.556	2.49351	0.0720785
165.819	2.18285	0.0674434
166.082	2.16202	0.0671209
166.345	2.16178	0.0671209
166.608	2.07684	0.0657819
166.871	2.07195	0.0657159
167.134	1.94511	0.0636696
167.397	2.03726	0.0651521
167.660	1.92917	0.0633963
167.923	1.91410	0.0631563
168.186	1.94976	0.0637377
168.449	1.93750	0.0635331
168.712	1.93518	0.0634990
168.975	1.84351	0.0619770
169.238	1.90833	0.0630531
169.501	1.87452	0.0625000
169.764	1.90000	0.0629153
170.027	1.81851	0.0615554
170.290	1.81851	0.0615554

Data Availability Statement

The PHEBUS PDS4 data products used in the study are from BepiColombo PHEBUS Team (2022) and available at https://doi.org/10.21413/phebus-euv-mercury_l1A_v0.1_latmos. The three observations of the first sequence correspond to the file: urn:esa:psa:bc_mpo_phebus:data_partially_processed:phe_par_sc_euvn_XODD_20211009T013000_20211009T022300:0.1.

The three observations of the second sequence corresponds to the file: urn:esa:psa:bc_mpo_phebus:data_partially_processed:phe_par_sc_euvn_XODD_20211009T233000_20211010T002300:0.1.

Acknowledgments
The BepiColombo mission to explore Mercury is an international cooperation between the European Space Agency, ESA, and the Japan Aerospace Exploration Agency, JAXA. The PHEBUS project is funded by National Space Agencies of France (CNES), Japan and Russia (Roscosmos). The ground calibrations were supported by the Italian Space Agency under the contracts ASI-INAF I/022/10/0 and ASI-INAF 2017-47-H.0.

References

Applin, D. M., Izawa, M. R. M., Cloutis, E. A., Gillis-Davis, J. J., Pitman, K. M., Roush, T. L., et al. (2018). Ultraviolet spectral reflectance of carboneous materials. *Icarus*, *307*, 40–82. https://doi.org/10.1016/j.icarus.2018.02.012

BepiColombo PHEBUS Team. (2022). Level 1A BepiColombo/PHEBUS EUV observations of the disk-integrated solar reflected light from the Mercury surface (Version 0.1) [Dataset]. LATMOS. https://doi.org/10.21413/PHEBUS-EUV-MERCURY_L1A_V0.1_LATMOS

Chassefière, E., Maria, J.-L., Goutail, J.-P., Quémerais, E., Leblanc, F., Okano, S., et al. (2010). PHEBUS: A double ultraviolet spectrometer to observe Mercury's exosphere. *Planetary and Space Science*, *58*(1–2), 201–223. https://doi.org/10.1016/j.pss.2008.05.018

Cintala, M. J. (1992). Impact-induced thermal effects in the lunar and Mercurian regoliths. *Journal of Geophysical Research*, *97*(E1), 947–973. https://doi.org/10.1029/91je02207

Cremonese, G., Sprague, A., Warell, J., Thomas, N., & Ksamfomality, L. (2007). The surface of Mercury as seen by Mariner 10. *Space Science Reviews*, *132*(2–4), 291–306. https://doi.org/10.1007/s11214-007-9231-1

Danjon, A. (1949). Photometrie et colorimétrie des planètes Mercure et Vénus. *Bulletin Astronomique*, *14*, 315–345.

Domingue, D. L., Chapman, C. R., Killen, R. M., Zurbuchen, T. H., Gilbert, J. A., Sarantos, M., et al. (2014). Mercury's weather-beaten surface: Understanding Mercury in the context of lunar and asteroidal space weathering studies. *Space Science Reviews*, *181*(1–4), 121–214. https://doi.org/10.1007/s11214-014-0039-5

Domingue, D. L., Vilas, F., Holsclaw, G. M., Warell, J., Izenberg, N. R., Murchie, S. L., et al. (2010). Whole-disk spectrophotometric properties of Mercury: Synthesis of MESSENGER and ground-based observations. *Icarus*, *209*(1), 101–124. https://doi.org/10.1016/j.icarus.2010.02.022

Eparvier, F. G., Chamberlin, P. C., Woods, T. N., & Thiemann, E. M. B. (2015). The solar extreme ultraviolet Monitor for MAVEN. *Space Science Reviews*, *195*(1–4), 293–301. https://doi.org/10.1007/s11214-015-0195-2

Flynn, B. C., Vallerga, J. V., Gladstone, G. R., & Edelstein, J. (1998). Lunar reflectivity from extreme ultraviolet explorer imaging and spectroscopy of the full Moon. *Geophysical Research Letters*, *25*(17), 3253–3256. https://doi.org/10.1029/98gl02483

Gladstone, G. R., McDonald, J. S., Boyd, W. T., & Bowyer, S. (1994). EUVE photometric observations of the Moon. *Geophysical Research Letters*, *21*(6), 461–464. https://doi.org/10.1029/93gl03290

Gladstone, G. R., Retherford, K. D., Egan, A. F., Kaufmann, D. E., Miles, P. F., Parker, J. W., et al. (2012). Far-ultraviolet reflectance properties of the Moon's permanently shadowed regions. *Journal of Geophysical Research*, *117*(E12), E00H04. https://doi.org/10.1029/2011JE003913

Hapke, B. (1963). A theoretical photometric function for the lunar surface. *Journal of Geophysical Research*, *68*(15), 4571–4586. https://doi.org/10.1029/jz068i015p04571

Hapke, B. (1966). An improved theoretical lunar photometry function. *The Astrophysical Journal*, *71*, 333–339.

Hapke, B. (1977). Interpretations of optical observations of Mercury and the Moon. *Physics of the Earth and Planetary Interiors*, *15*(2–3), 264–274. https://doi.org/10.1016/0031-9201(77)90035-8

Hapke, B. (1981). Bidirectional reflectance spectroscopy 1. Theory. *Journal of Geophysical Research*, *86*(B4), 3039–3054. https://doi.org/10.1029/jb086ib04p03039

Hapke, B. (2001). Space weathering from Mercury to the asteroid belt. *Journal of Geophysical Research*, *106*(E5), 10039–10073. https://doi.org/10.1029/2000je001338

Hapke, B. (2012). *Theory of reflectance and emittance spectroscopy* (2nd ed.). Cambridge University Press.

Hendrix, A. R., Domingue, D. I., & Noll, K. S. (2012). *Ultraviolet properties of planetary ices, in the science of solar system ices* (Vol. 356). Astrophysics and Space Science Library.

Hendrix, A. R., Filacchione, G., Paranicas, C., Schenk, P., & Scipioni, F. (2018). Icy Saturnian satellites: Disk-integrated UV-IR characteristics and links to exogenic processes. *Icarus*, *300*, 103–114. https://doi.org/10.1016/j.icarus.2017.08.037

Hendrix, A. R., Greathouse, T. K., Retherford, K. D., Mandt, K. E., Gladstone, G. R., Kaufmann, D. E., et al. (2016). Lunar swirls: Far-UV characteristics. *Icarus*, *273*, 68–74. https://doi.org/10.1016/j.icarus.2016.01.003

Hendrix, A. R., Retherford, K. D., Gladstone, G. R., Hurley, D. M., Feldman, P. D., Egan, A. F., et al. (2012). The lunar far-UV albedo: Indicator of hydration and weathering. *Journal of Geophysical Research*, *117*(E12), E12001. https://doi.org/10.1029/2012JE0045252

Hendrix, A. R., & Vilas, F. (2006). The effects of space weathering at UV wavelengths: S-class asteroids. *The Astrophysical Journal*, *132*(3), 1396–1404. https://doi.org/10.1086/506426

Holsclaw, G. M., McClintock, W. E., Domingue, D. L., Izenberg, N. R., Blewett, D. T., & Sprague, A. L. (2010). A comparison of the ultraviolet to near-infrared spectral properties of Mercury and the Moon as observed by MESSENGER. *Icarus*, *209*(1), 179–194. https://doi.org/10.1016/j.icarus.2010.05.001

Irvine, W., Simon, T., Menzel, D., Pikoos, C., & Young, A. (1968). Multicolor photoelectric photometry of the brighter planets. 3 Observations from Boyden Observatory. *The Astronomical Journal*, *73*, 807–828.

Izenberg, N. R., Klima, R. L., Murchie, S. L., Blewett, D. T., Holsclaw, G. M., McClintock, W. E., et al. (2014). The low-iron reduced surface of Mercury as seen in spectral reflectance by MESSENGER. *Icarus*, *228*, 364–374. https://doi.org/10.1016/j.icarus.2013.10.023

Lawrence, D. J., Feldman, W. C., Elphic, R. C., Little, R. C., Prettyman, T. H., Maurice, S., et al. (2002). Iron abundances on the lunar surfaces as measured by the Lunar Prospector gamma-ray and neutron spectrometers. *Journal of Geophysical Research*, *107*(E12), 5130–13-26. https://doi.org/10.1029/2001JE001530

Lucey, P. G., & Riner, M. A. (2011). The optical effects of small iron particles that darken but do not redden: Evidence of intense space weathering on Mercury. *Icarus*, *212*(2), 451–462. https://doi.org/10.1016/j.icarus.2011.01.022

Lucke, R. L., Henry, R. C., & Fastie, W. G. (1976). Far-ultraviolet albedo of the Moon. *The Astrophysical Journal*, *81*, 1162–1169. https://doi.org/10.1086/112000

Mallama, A., Wang, D., & Howard, R. A. (2002). Photometry of Mercury from SOHO/LASCO and Earth, the phase function from 2 to 170°. *Icarus*, *155*, 253–264. https://doi.org/10.1006/icar.2001.6723

McClintock, W. E., Izenberg, N. R., Holsclaw, G. M., Blewett, D. T., Domingue, D. L., Head, J. W., III, et al. (2008). Spectroscopic observations of Mercury's surface reflectance during MESSENGER's first Mercury flyby. *Science*, *321*(5885), 62–65. https://doi.org/10.1126/science.1159933

Murchie, S. L., Klima, R. L., Izenberg, N. R., Domingue, D. L., Blewett, D. T., & Helbert, J. (2018). Spectral reflectance constraints on the composition and evolution of Mercury's surface. In S. Solomon, L. Nittler, & B. Anderson (Eds.), *Mercury: The view after MESSENGER* (pp. 191–215). Cambridge Planetary Science, Cambridge University Press.

Peplowski, P. N., Klima, R. L., Lawrence, D. J., Ernst, C. M., Denevi, B. W., Frank, E. A., et al. (2016). Remote sensing evidence for an ancient carbon-bearing crust on Mercury. *Nature Geoscience*, *9*(4), 273–276. https://doi.org/10.1038/ngeo2669

Philipp, H. R. (1985). Silicon dioxide (SiO_2) (glass). In E. D. Palik (Ed.), *Handbook of optical constants of solids* (pp. 749–763). Academic Press.

Pieters, C. M., & Noble, S. K. (2016). Space weathering on airless bodies. *Journal of Geophysical Research: Planets*, *121*(10), 1865–1884. https://doi.org/10.1002/2016JE005128

Quémerais, E., Chaufray, J.-Y., Koutroumpa, D., Leblanc, F., Réberac, A., Lustrement, B., et al. (2020). PHEBUS on Bepi-Colombo: Post-launch update and instrument performance. *Space Science Reviews*, *216*(4), 67. https://doi.org/10.1007/s11214-020-00695-6

Quémerais, E., Sandel, B. R., Izmodenov, V. V., & Gladstone, R. G. (2013). Thirty years of interplanetary background data: A global view. In E. Quémerais, M. Snow, & R.-M. Bonnet (eds.) *Cross-calibrations of far UV spectra of solar system objects and heliosphere ISSI scientific reports series* (Vol. 13, pp. 141–162).

Rava, B., & Hapke, B. (1987). An analysis of the Mariner 10 color ratio map of Mercury. *Icarus*, *71*(3), 397–429. https://doi.org/10.1016/0019-1035(87)90037-6

Snow, M., Reberac, A., Quémerais, E., Clarke, J., McClintock, W. E., & Woods, T. N. (2013). A new catalog of ultraviolet stellar spectra for calibration. In E. Quémerais, M. Snow, & R.-M. Bonnet (Eds.), *Cross-calibrations of far UV spectra of solar system objects and heliosphere, ISSI scientific reports series* (Vol. 13, pp. 191–223).

Syal, M. B., Schultz, P. H., & Riner, M. A. (2015). Darkening of Mercury's surface by cometary carbon. *Nature Geoscience*, *8*(5), 352–356. https://doi.org/10.1038/ngeo2397

Thuillier, G., Floyd, L., Woods, T. N., Cebula, R., Hilsenrath, E., Hersé, M., & Labs, D. (2004). Solar irradiance reference spectra for two solar active levels. *Advances in Space Research*, *34*(2), 256–261. https://doi.org/10.1016/j.asr.2002.12.004

Trang, D., Lucey, P. G., & Izenberg, N. R. (2017). Radiative transfer modeling of MESSENGER VIRS spectra: Detection and mapping of submicroscopic iron and carbon. *Icarus*, *293*, 206–217. https://doi.org/10.1016/j.icarus.2017.04.026

Vilas, F. (1988). Surface composition of Mercury from reflectance spectrophotometry. In F. Vilas, C. Chapman, & M. Matthews (Eds.), *Mercury* (pp. 59–76). University of Arizona Press.

Vilas, F., Domingue, D. L., Helbert, J., D'Amore, M., Maturilli, A., Klima, R. L., et al. (2016). Mineralogical indicators of Mercury's hollows composition in MESSENGER color observations. *Geophysical Research Letters*, *43*(4), 1450–1456. https://doi.org/10.1002/2015gl067515

Warell, J., & Valegard, P.-G. (2006). Albedo-color distribution on Mercury. A photometric study of the poorly known hemisphere. *Astronomy & Astrophysics*, *460*(2), 625–633. https://doi.org/10.1051/0004-6361:20065850

Woods, T. N., Chamberlin, P. C., Harder, J. W., Hock, R. A., Snow, M., Eparvier, F. G., et al. (2009). Solar irradiance reference spectra (SIRS) for the 2008 Whole Heliosphere interval (WHI). *Geophysical Research Letters*, *36*(1), L01101. https://doi.org/10.1029/2008GL036373

Woods, T. N., Eparvier, F. G., Bailey, S. M., Chamberlin, P. C., Lean, J., Rottman, G. J., et al. (2005). Solar EUV Experiment (SEE): Mission overview and first results. *Journal of Geophysical Research*, *110*(A1), A01312. https://doi.org/10.1029/2004ja010765

Woods, T. N., Eparvier, F. G., Hock, R., Jones, A. R., Woodraska, D., Judge, D., et al. (2012). Extreme Ultraviolet Variability Experiment (EVE) on the Solar Dynamics Observatory (SDO): Overview of science objectives, instrument design, data products and model developments. *Solar Physics*, *275*(1–2), 115–143. https://doi.org/10.1007/s11207-009-9487-6

Wu, H. H., & Broadfoot, A. L. (1977). The extreme ultraviolet albedos of the planet Mercury and of the Moon. *Journal of Geophysical Research*, *82*(5), 759–761. https://doi.org/10.1029/jb082i005p00759